Supplement of The Cryosphere, 12, 549–564, 2018
https://doi.org/10.5194/tc-12-549-2018-supplement

The Cryosphere Open Access EGU

Supplement of

Sub-seasonal thaw slump mass wasting is not consistently energy limited at the landscape scale

Simon Zwieback et al.

Correspondence to: Irena Hajnsek (hajnsek@ifu.baug.ethz.ch)

S1 Detailed methods

S1.1 Seasonal elevation loss rate

We estimated the average elevation loss rate r_s of every resolution cell by temporally averaging multiple height change estimates. The temporal stacking had two advantages: it provided a single quantity to characterize a pixel's elevation loss and it reduced the uncertainty. r_s was estimated by generalized least squares and so accounted for the temporally varying accuracy of the rate estimates and their correlations.

Before optimally combining multiple estimates, the uncertainty of the individual sub-seasonal elevation loss rate estimates had to be known. It was derived from that of the interferometric phases, which in turn was estimated from the observed coherence magnitude [5]. The phase noise in a single interferogram is inversely related to the coherence magnitude, as predicted by the Cramer-Rao bound of the standard error [6]

$$\sigma_\phi = \frac{1}{\sqrt{2L}} \frac{\sqrt{1-\gamma^2}}{\gamma} \tag{S1}$$

where L is the effective number of looks after range spectral filtering. The standard error of the height estimate was then computed using $\sigma_h = k_z^{-1}\sigma_\phi$. This uncertainty was then used to estimate that of the height changes $\Delta h(t_i, t_{i+1})$ between two acquisitions at times t_i and t_{i+1}. We did this using the following stochastic model, expressed in terms of the true height change $\Delta h(t_i, t_{i+1})$

$$r(t_i, t_{i+1}) = -\frac{1}{t_{i+1} - t_i} \left(\Delta h(t_i, t_{i+1}) + \varepsilon_{h(t_{i+1})} - \varepsilon_{h(t_{i+1})} \right) \tag{S2}$$

where $\varepsilon_{h(t_{i+1})}$ represented the error at time t_{i+1}, i.e. a zero-mean random variable with standard deviation $\sigma_{h(t_{i+1})}$. The height errors $\varepsilon_{h(t_{i+1})}$ were assumed not correlated between acquisitions [10]. The accuracy of these uncertainty estimates will be assessed in Sec. S1.3.

The stacked elevation loss rate r_s was computed from the time series of estimates $r(t_i, t_{i+1})$ assuming a constant rate. The design matrix in the generalized least-squares approach was given by a vector of all ones. The stochastic information was given by the uncertainty estimates derived from Eq. (S2). The model fitting gave the average elevation loss rate r_s as well as its standard error. The estimate of this standard error could in theory be refined by estimating the overall noise level from the residuals, but it was deemed too noisy because of the small number of TanDEM-X acquisitions. However, such an estimation allowed us to test the accuracy of the uncertainty models (Sec. S1.3).

S1.2 Biases in height change estimates

Deviations between the observed Δh and the actual mean elevation changes between two interferogram acquisitions can arise because the phase centre in an interferogram does not represent the mean elevation height. In the main document, we draw attention to the bias caused by snowmelt and vegetation phenology, and to the influence of water bodies. We now provide a more detailed assessment of these three error sources, before analysing those associated with sub-resolution heterogeneity and geometric distortions.

Snowmelt was found to induce spurious measurements of ground surface elevation loss. Fig. S1a shows TanDEM-X height changes of around 1 metre between early June, when late-lying snow banks in gullies and at breaks in slopes were still widespread on Kurungnakh, and late June, when they had largely disappeared. The observed elevation loss suggests that the TanDEM-X height measurement was located close to the top of the presumably wet or refrozen snow pack, consistent with results from glaciology [2]. As snow packs often accumulate at locations where rapid permafrost degradation is expected (e.g. breaks in slope at slumps), the apparent elevation loss may be misinterpreted as mass wasting; areas with residual snow cover should hence be discarded.

Dense shrub cover was found to be associated with apparent height changes during the summer season. In the Tuktoyaktuk coastlands, we observed apparent elevation increases of around 30-60 cm in early summer in areas covered by tall and dense deciduous

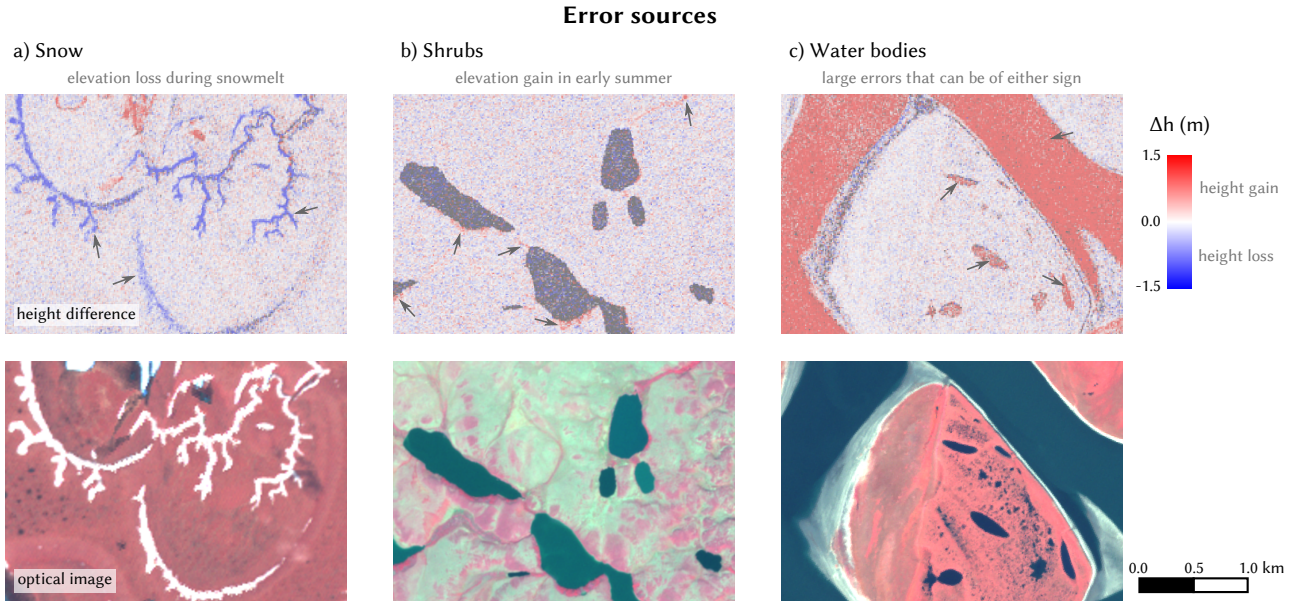

Figure S1: Error sources in the tundra are made evident by non-zero height changes Δh (top row) occurring in discrete locations associated with specific land cover (optical images in the bottom row). a) Apparent subsidence on Kurungnakh between 08 June and 30 June occurs over snowbanks (arrows) that are clearly visible in the ASTER image from 15 June. b) Apparent uplift in the Tuktoyaktuk coastlands between 01 June and 15 July over dense shrub patches that are marked by a high near infrared reflectance (shown in red) in a Sentinel-2 image from 2016. c) Spurious height changes from 13 August to 24 August over water surfaces such as lakes or a river branch on Samoylov, an island close to Kurungnakh. The water bodies, including polygonal ponds, are characterized by their dark appearance in a 2016 Sentinel-2 image. Water-induced errors are also visible in a). The Δh images also indicate the uncertainty of the estimates, with black areas corresponding to low accuracies.

shrubs (Fig. S1b). Conversely, we found only very limited shrub-induced biases in July and August (see Fig. 3). The observed elevation increase was likely mainly related to phenological changes (moisture, leaf growth in early summer) rather than changes in height owing to the magnitude of the change [11]. As dense shrub cover is commonly encountered in permafrost disturbances like gullies or stabilized slumps [7], the phenology may hence mask actual surface elevation decreases in early summer.

Over water surfaces, the observed phase was influenced by surface waves due to the non-zero along-track baseline (Eq. 1), cf. [6, 12]. Changing wind conditions and currents translated to apparent height changes of several metres over water surfaces in some of our data (Fig. S1c). As the inferred Δh were essentially useless, these areas would have had to be masked if we had not delineated thermokarst disturbances manually. What caused more concern were sub-resolution water bodies, which are widespread in lowland tundra regions. Spurious height changes were also seen over polygonal terrain, but they were subtle (Fig. S1c). We chose a different approach to detect these errors by looking at time series of observed height changes. This approach was based on the model predictions in Fig. S2a), according to which the wave-induced phase contribution is expected to be larger over lakes than over terrain with sub-resolution waterbodies, but of the same sign, for an entire time series . We hence expected the observed Δh to be temporally correlated with those over lakes, and such a positive correlation, albeit weak, was indeed observed (Fig. S3). This error source is not expected to be relevant for the hillslope disturbances studied here, but it will have to be considered when studying lowland thermokarst and gullies with surface flow.

We now focus on errors that are related to the heterogeneity within the resolution cell and to geometric distortions. When all parts of the resolution cell scatter equally strongly (in an effective sense that accounts for the distortions due to the slant-range geometry), the height measurement will reflect the average surface height, and differences therein the volumetric height change. A simple illustration is depicted in Fig. S2c, which shows a retreating scarp observed along the strike direction. Assuming the scarp and the terraces above and below to scatter equally, the interferometrically determined height $\hat{h}$ is expected to be equal to the average geometric height $\bar{z}$

$$\hat{h} = \frac{1}{k_z} \arg \int_0^a \mathrm{e}^{\mathrm{i}k_z z(x)} \mathrm{d}x = \frac{1}{k_z} \arg \mathrm{e}^{\mathrm{i}k_z \bar{z}} \cdot \int_0^a \mathrm{e}^{\mathrm{i}k_z (z(x)-\bar{z})} \mathrm{d}x \overset{z-\bar{z} \ll \frac{2\pi}{k_z}}{\approx} \bar{z} \tag{S3}$$

However, this relation breaks down in heterogeneous resolution cells.

The presence of multiple surface covers, such as undisturbed moss and disturbed mineral soil, complicates the interpretation of the radar data as the aggregation process for the complex coherence depends on the size, slope and reflectivity of the surfaces present within the resolution cell. To assess the induced errors, we modelled the complex coherence and from it the height estimates of an ablating inclined scarp using the backscattering coefficients observed in adjacent pixels [13]. As the headwall retreats, the weakly reflecting mossy upland tundra is replaced by a disturbed, more strongly reflecting surface. The latter will 'pull' the phase centre down to a larger extent than the reduction in the mean geometric height (Fig. S4). A second effect, which depends on the orientation of the

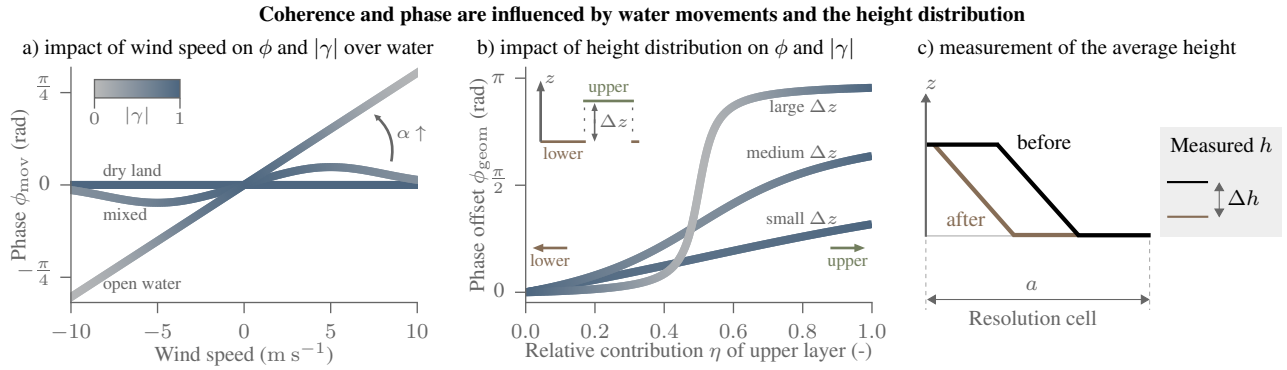

Figure S2: Surface characteristics influence the observed coherence and can also contribute to the phase. a) Over water surfaces, wind-induced movements lead to changes of the surface structure during the effective along-track time separation of around 0.01 s, causing decorrelation and phase offsets ϕ_{mov}. The predictions are based on the model by [3] when the look direction and the wind direction coincide; for mixed pixels, the land and water contributions are assumed to add incoherently, with the relative contribution of water being denoted by α. b) A distribution of heights within the resolution cell (e.g. irregular topography, vegetation) causes geometric decorrelation. For the simple two-layer model, the loss of coherence and the geometric phase contribution ϕ_{geom} depend on the relative backscatter contribution of the two layers η and on the height difference Δz with respect to $\frac{1}{k_z}$. c) The measured height h is approximately equal to the average height according to Eq. S3 for equal scattering contributions from all surfaces, here illustrated for a retreating scarp (looking along the strike direction).

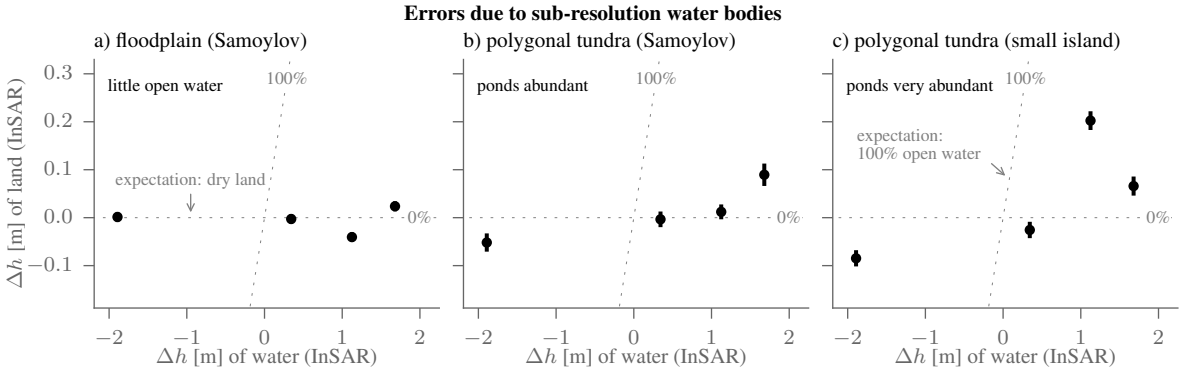

Figure S3: A bias induced by the presence of subsurface waterbodies is indicated by the temporal relation between Δh over different tundra types (vertical axis; mean $\pm$ 2 standard errors) and a nearby lake (horizontal axis; mean, uncertainty too small to be evident). The magnitude of the relation increases with the abundance of waterbodies (from left to right). All three locations are around 5 km northeast of Kurungnakh island.

slump with respect to the look direction, is due to the changing projection into the slant-range geometry. The overall bias was found to be very sensitive to the position of the headwall within the resolution cell (Fig. S4). However, for an incremental retreat of the headwall, it was predicted to largely average out when aggregating multiple resolution cells. Another source of bias in heterogeneous resolution cells may arise due to temporal changes in the surface reflectivity, e.g. due to changing surface moisture. In wet conditions, the backscattering coefficients of both upland tundra and the disturbed areas were found to increase (by around 0.5 dB and 1.0 dB). Due to the stronger 'pulling' effect of the disturbed area, the estimated height decreases even when the headwall position remains constant. However, we estimated this effect to be small ($\approx$ 10 cm), but it may be temporally correlated with moisture conditions and precipitation.

The role of geometric distortions was also assessed by the comparison of observations from different orbits. In theory, incompatible estimates of the same area could for instance be induced by the partial shadowing within a resolution cell at a scarp when the radar looks downslope rather than upslope. We found for the slumps in the overlap area in the Tuktoyaktuk coastlands area that the estimated rates were generally consistent within the noise level (Fig. S5). Arguably, the hilly rather than mountainous terrain and the manual delineation of the active areas, which discarded e.g. layover areas with unreliable estimates, helped to limit the influence of the geometric distortions.

S1.3 Uncertainty analysis at the pixel level

We now give a detailed description of how we assessed the accuracy of the uncertainty estimates of the estimated height changes Δh for each pixel. Such an independent assessment was deemed necessary as the internal uncertainty estimates relied on two types of

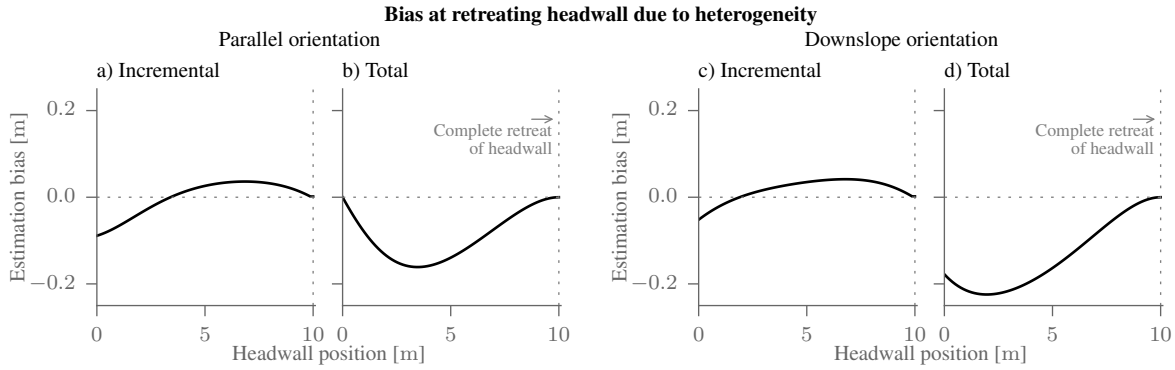

Figure S4: Bias of the InSAR-derived Δh compared to the true volumetric height change for a retreating headwall. It is induced by the higher backscattering from the disturbed slope compared to the undisturbed upland surface (headwall height of 5 m, representative backscatter values) and also due to the changing projection into the slant-range geometry. Initially, the entire resolution cell is covered by undisturbed tundra (headwall position = 0). As the headwall retreats across the resolution cell (horizontal axis), the height change is underestimated (i.e. the elevation loss overestimated) for both an incremental 1 m retreat of the headwall (a,c) and for the total (b,d) retreat, i.e. when compared to the initial situation. For the incremental retreat, the bias changes sign after 2-5 m of headwall retreat. The radar system parameters match those of the descending orbit (Tuktoyaktuk coastlands).

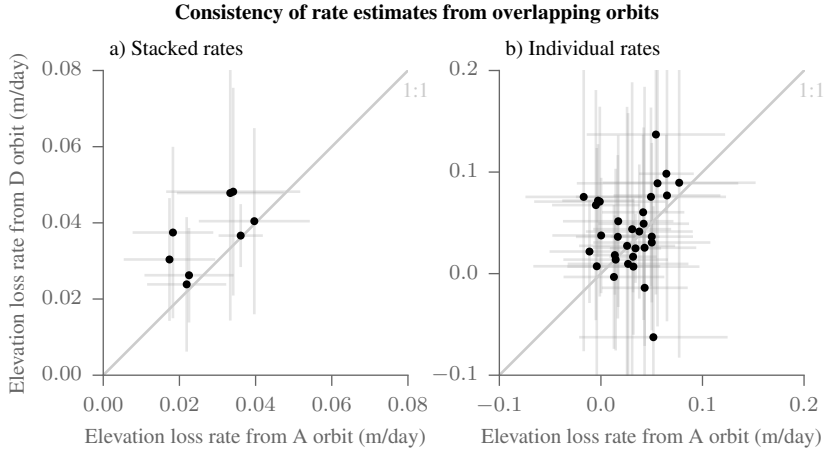

Figure S5: Crossover-analysis from the ascending and descending orbit of the observed elevation loss rates in the overlap area in the Mackenzie Delta area. The mean (stacked) rates in July and August in a) and the individual 11 day rate estimates in b) are broadly consistent.

assumptions: i) those related to the model of the phase noise that only considers decorrelation, and ii) the lack of consideration of errors unrelated to decorrelation. Assumptions i) include the reliance on the Gaussian speckle model and on the approximate Cramer Rao bound, and the fact that the coherence magnitude $|\gamma|$ was not known but had to be estimated to the data. The assessment of their impact on the estimates of the decorrelation-induced uncertainty required a data-driven approach.

Before turning to the decorrelation-induced error, we first show that all non-decorrelation error sources, i.e. inaccuracies due to assumptions ii), were negligible by comparison. Quantitatively, they were estimated to be at least an order of magnitude smaller than the noise error of 30-60 cm (Fig. S6). The first neglected error source was due to inaccuracies in the baseline information: it was estimated to be well below 1 mm for a typical relief of 100 m [6]. Secondly, the errors induced by inaccurate referencing of the height were also found to be much smaller than the noise level. This was indicated by the analysis over stable areas, from which a very conservative estimate of around 2 cm was obtained by attributing all the observed height change (also due to noise and actual movements) to a reference error (Fig. S6). Thirdly, phase unwrapping errors could lead to large errors of either sign, but they did not occur in our approach based on interferogram differencing as the observed height changes over the short temporal intervals were small compared to the height of ambiguity. Finally, it neglected an error in the reference DEM, which our approach based on the differencing of the wrapped phases required to account for the small differences in k_z between two acquisitions. According to Eq. 1, such an error δh induced an error in the estimated height difference of $\Delta k_z \delta h$. A representative difference in k_z of $\frac{\delta k_z}{k_z} \approx 0.1\%$ corresponds to an error of 3 cm assuming a conservative DEM accuracy of 30 m.

To assess the validity of the coherence-based uncertainty estimates, we directly compared them to observations [10, 9]. Our analyses indicated that these uncertainty estimates were reliable to within 30%, with a tendency of being conservative, i.e. on the safe side. The assessment was conducted in two ways that were based on different assumptions about the spatial or temporal characteristics of the height changes.

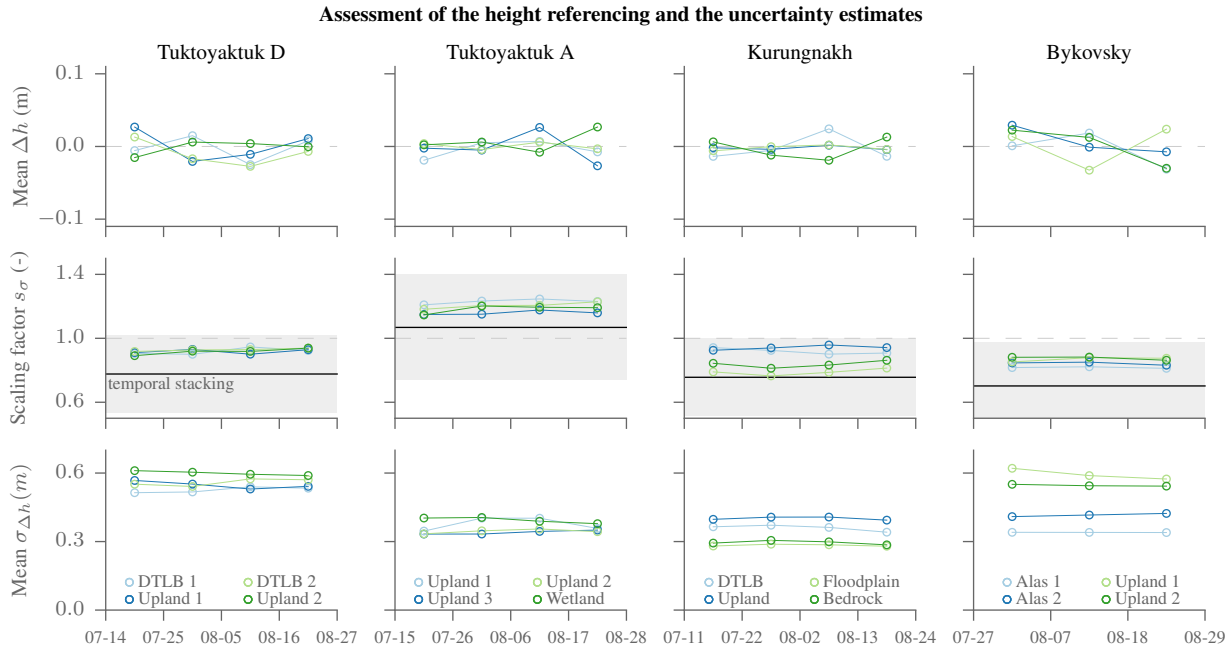

Figure S6: Assessment of the height referencing and of the coherence-based uncertainty estimates over stable areas in all study regions (columns). The height referencing is accurate to within around 2 cm, as indicated by the observed mean height changes within the stable areas (top row); standard deviation of these estimates is 1-2 cm). The coherence-based uncertainty estimates are compared to the variability within the stable areas (e.g. drained thaw lake basins, DTLB) and to the temporal variability of all land pixels across (second row). The variability-based estimates are expressed as a scaling-factor s, with $s < 1$ indicating smaller variability than expected based on the coherence, i.e. conservative estimates. Stability factors < 1 are observed in around 75% of the cases. The standard deviation within the stable areas is shown in the third row, yielding values of 30-60 cm.

First, we analysed the observed spatial variability of Δh in stable regions, which should only be due to noise in a perfectly homogeneous area [10]. From the observed spatial variability within a window, we derived an alternative estimate of the overall magnitude of the noise, which could then be compared to the coherence-based one. We did this using a generalized least-squares approach. It was almost identical to that for temporal stacking discussed in Sec. S1.1, but applied to a spatial window rather than a time series. It required as input the relative uncertainty of the height changes within the window for each interferogram, which we modelled using the Cramer-Rao phase noise estimate assuming no spatial auto-correlation. We then derived an absolute noise standard deviation from the observed variability and compared it to what was expected based on the coherence-based pixel-level uncertainties: their ratio was expressed as a scaling factor s_σ. A value of s_σ less than one, i.e. when the stability-based uncertainty estimate is smaller than the original one, indicates that the coherence-based estimates are conservative. We observed this in 75% of the studied stable areas (Fig. S6). The estimated s_σ was based on two crucial assumptions. First, the homogeneity of the stable regions in terms of their height changes: a violation of this assumption would lead to an overestimation of s_σ (i.e. a conservative estimate). Second, the absence of spatial auto-correlation; positive auto-correlation would lead to an underestimation of s_σ. However, auto-correlation is typically not considered a problem [9] and also we found little indication of auto-correlation: the estimated auto-correlation length in the stable areas was considerably smaller than the resolution of the multi-looked product (3.0 ± 0.9 m vs 12 m).

Second, we derived an estimate of the noise level by analysing the temporal variability of Δh for each pixel. In order for this estimate to be valid, we had to assume that the rate of height change was constant. This critical assumption was not the only problem, as the brevity of the time series precluded the robust estimation of the absolute noise level. The estimation itself was based on the temporal least-squares stacking of Sec. S1.1. Like for the spatial analysis, we expressed the new estimate of the standard error in terms of a scaling factor s_σ. Over land, the distribution of s_σ turned out to be fairly broad (median absolute deviation of around 0.3). The median values of the four analysed regions were comparable to those found using the spatial analysis (but a bit lower, between 0.7 and 1.1; Fig. S6). In summary, the two data-driven assessment showed that the coherence-based uncertainty estimates were reliable, if a little conservative.

S1.4 Uncertainty analysis at the landform level

We now describe how these pixel-level elevation changes and their uncertainties were spatially aggregated to produce mean values for each thaw slump. The key advantage of spatial aggregation is that the noise level can be reduced. The aggregation was conducted by forming the median within the manually delineated active part of the landform. We opted for the median because it is less susceptible to outliers, but for the most part the results for the mean are similar (relative differences across all slumps of $4 \pm 6\%$).

We estimated the uncertainty of the aggregated height changes by parameteric bootstrapping. Bootstrapping is a popular method

for characterizing the sampling properties – e.g. the standard error – for estimators in a computer-intensive way that is based on sampling [1]. Its key idea is to approximate the unknown distribution behind the data by an estimate derived from the data and to use this distribution to simulate the data-generating process. Here, we applied it to the spatially aggregated rates and we approximated the unknown distribution of the data by assuming that the noise could be described by the coherence-based error estimates. Specifically, we assumed that the noise was not spatially auto-correlated and that it could be approximated by a Gaussian distribution with a standard deviation given by (S1) [5]. The true rate, i.e. the expected value of the distribution, was estimated from the data. From the distribution of the data for each pixel within the landform, we drew $B = 1000$ random samples, computed the aggregate of each sample and estimated the standard error across the B samples [1].

S1.5 Hypothesis tests of deformation time series

Were the observed elevation loss dynamics consistent with the hypothesized energy-limited ablation losses? The uncertainty in the estimated height changes suggests the use of statistical hypothesis testing to address this question. To this end, we employed parametric bootstrap testing, similar to the characterization of the aggregate uncertainties [1]. The test statistic measures the deviation of the observed time series $r(t_i, t_{i+1})$ from the hypothesized one $r_h(t_i, t_{i+1})$. The test statistic D was based on normalized rates:

$$D = \sum_{i=1}^{N-1} \left| \frac{r(t_i, t_{i+1})}{\sum_{j=1}^{N-1} |r(t_j, t_{j+1})|} - \frac{r_h(t_i, t_{i+1})}{\sum_{j=1}^{N-1} |r_h(t_j, t_{j+1})|} \right| \tag{S4}$$

i.e. it measured the magnitude of the difference between rates normalized so that the absolute values sum to one. The idea of a statistical test is to analyse the distribution of D when the null hypothesis applies, i.e. when r tracks r_h, and compare this to the observed D. The distribution under the null hypothesis was not completely known, as the true time series $r(t_i, t_{i+1})$ was only prescribed by $r_h(t_i, t_{i+1})$ up to an unknown scale factor. In the bootstrapping approach, this scale factor was estimated (using least squares) and the noisy rate observations were sampled as in Sec. S1.4 to approximate the distribution of D [1]. The outcome of the test was reported as a p-value, which was estimated by counting the fraction of samples that exceeded the actually observed D. We did this not only for the energy balance model (assuming a horizontal surface), but also for a model of uniform rate.

S1.6 Clustering of deformation time series

To explore the synchronicity and temporal similarity of the height changes of the active landforms, fuzzy C-means clustering was employed [8]. It grouped all the landforms into clusters such that the members of the same cluster shared similar temporal evolutions. This clustering approach is fuzzy in that each landform l is not assigned into one and only one group c, but instead its association to all groups is characterized by a fractional degree of membership $u_{l,c}$. The landform's membership depends on its dissimilarity to all N_c cluster centres; the dissimilarity is quantified by a distance function [4].

The choice of the distance function is critical for a successful partitioning of the data. To make the algorithm insensitive to the overall magnitude, we used the statistic D of (S4). A second degree of freedom in the clustering was given by the degree of fuzziness m, which we set to 1.3 as recommended by [4].

C-means is an iterative algorithm that requires an initial membership allocation for all N_l landforms, which we determined randomly [4]. We repeated the initialization 100 times and chose the final clustering that minimized the total within-cluster dissimilarity J defined by [8]

$$J = \sum_{l=1}^{N_l} \sum_{c'=1}^{N_c} \left(u_{l,c'}\right)^m D^2(l, c') \tag{S5}$$

To compute the cluster centres and the memberships, the number of clusters N_c had to be prescribed. We did not prescribe it directly but rather inferred it from the data by performing the partitioning for several values of N_c and subsequently choosing a value that was in some sense optimal [8]. The quality of a partitioning is generally difficult to quantify, but most approaches focus on the total within-cluster dissimilarity J. This dissimilarity decreases with N_c as the clusters have to represent fewer landforms and thus become increasingly homogeneous. The value of J in itself is thus a poor indicator of the quality of the clustering, but the change of J with the number of clusters is [8]. Ideally, if one has found a parsimonious but representative partitioning, reducing the number of clusters should lead to sharp increase in J whereas increasing N_c should have little impact. The idea is hence to look for a kink or elbow in the curve of J vs N_c [8]. For the slumps in the Tuktoyaktuk coastlands, such a kink occurred at $N_c = 3$, but the choice was not clear-cut as minor ones also occurred at 5 and 7 clusters (Fig. S7). The plausibility of the partitioning into three clusters was also supported by the similar clustering results obtained when studying the ascending and descending orbits separately.

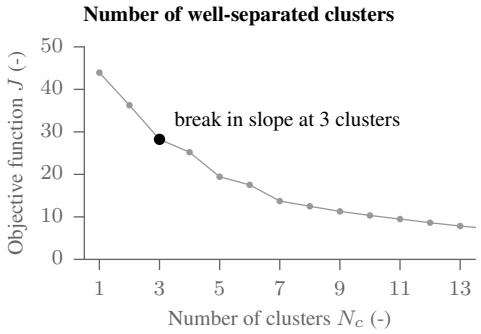

Figure S7: The within-cluster dissimilarity J decreases sharply at $N_c = 3$ clusters but barely changes when N_c is increased to four clusters. This suggests that three clusters provide a reasonable and parsimonious partitioning of the data.

S2 Additional material

	Study area			
Parameter	Tuktoyaktuk CL A	Tuktoyaktuk CL D	Kurungnakh	Bykovsky
Orbit direction	A	D	D	A
Number of acquisitions	7	5	8	6
CoSSc slant range resolution (m)	1.8	1.2	1.2	1.2
CoSSc azimuth resolution (m)	3.3	6.6	6.6	6.6
Polarization	VV	HH	HH	HH
Incidence angle (°)	46	38	25	35
Height of ambiguity (m)	14	14	8	11
Effective along-track time separation (ms)	12	7	10	9

Table S1: TanDEM-X data properties for all study sites and orbits. The Tuktoyaktuk coastlands were covered by two orbits. The orbit direction was either ascending (A) or descending (D) and the antenna always pointed to the right. The effective along-track time separation governs the sensitivity to surface movements, as described by [12].

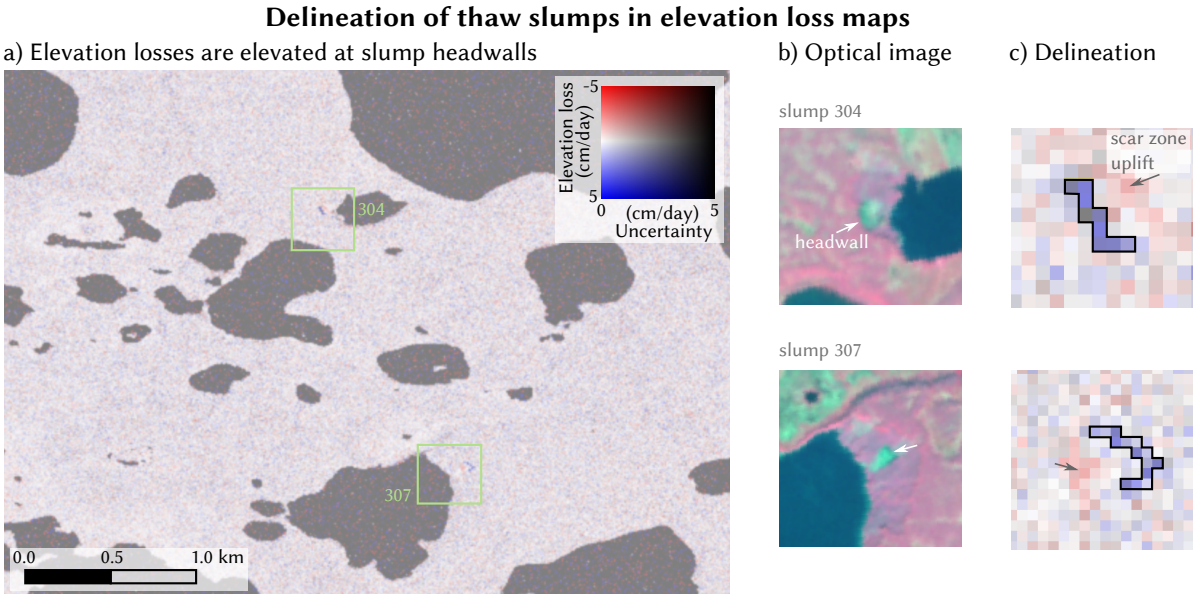

Figure S8: Manual delineation of the actively mass-wasting parts of landforms, shown here for thaw slumps in the Tuktoyaktuk Coastlands (lower left corner: 69.5 N 133.0 E). a) The stacked rate of volume losses is mostly close to zero over land, except where rapid permafrost degradation occurs as here at three thaw slumps (grey arrows). b) Sentinel-2 false colour image showing the two slumps highlighted in a), whose barely vegetated scar zone of mineral soil is clearly visible (greenish colour). c) Close-up of the elevation loss rate around two slumps: the manually delineated pixels around the headwall are shown with a black margin; the uplift on the slump floor is indicated with grey arrows.

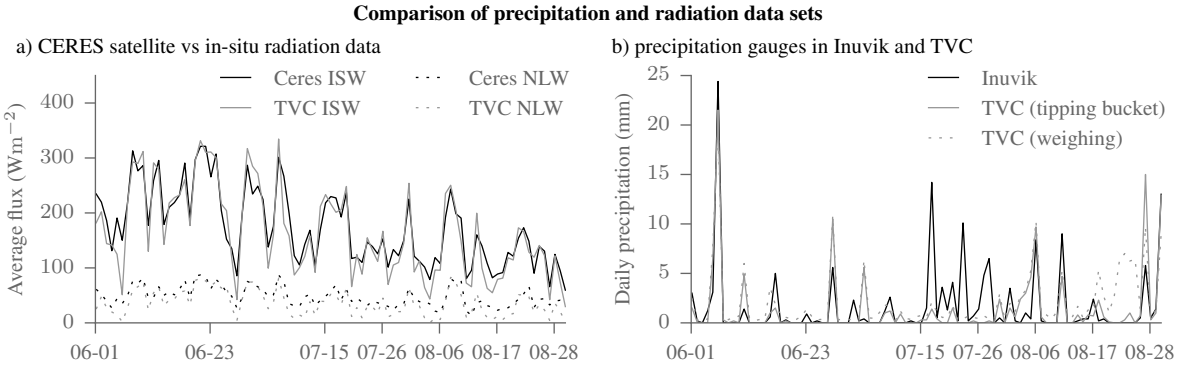

Figure S9: Comparison of the forcing data sets (Tuktoyaktuk coastlands). a) The incoming shortwave radiation (ISW) estimates in the CERES satellite data set and the in-situ measurements at Trail Valley Creek (TVC) match well: $R^2 = 0.89$, relative bias RB $= 5\%$. The net longwave radiation (LW) shows larger deviation: $R^2 = 0.77$, RB $= 25\%$. b) The precipitation data sets show large discrepancies. The manually read weighing gauge at Inuvik and the automatic tipping bucket gauge at TVC (45 km to the northeast) have $R^2 = 0.54$ and RB $= 18\%$. The collocated gauges at TVC match to with $R^2 = 0.81$ and RB $= 52\%$.

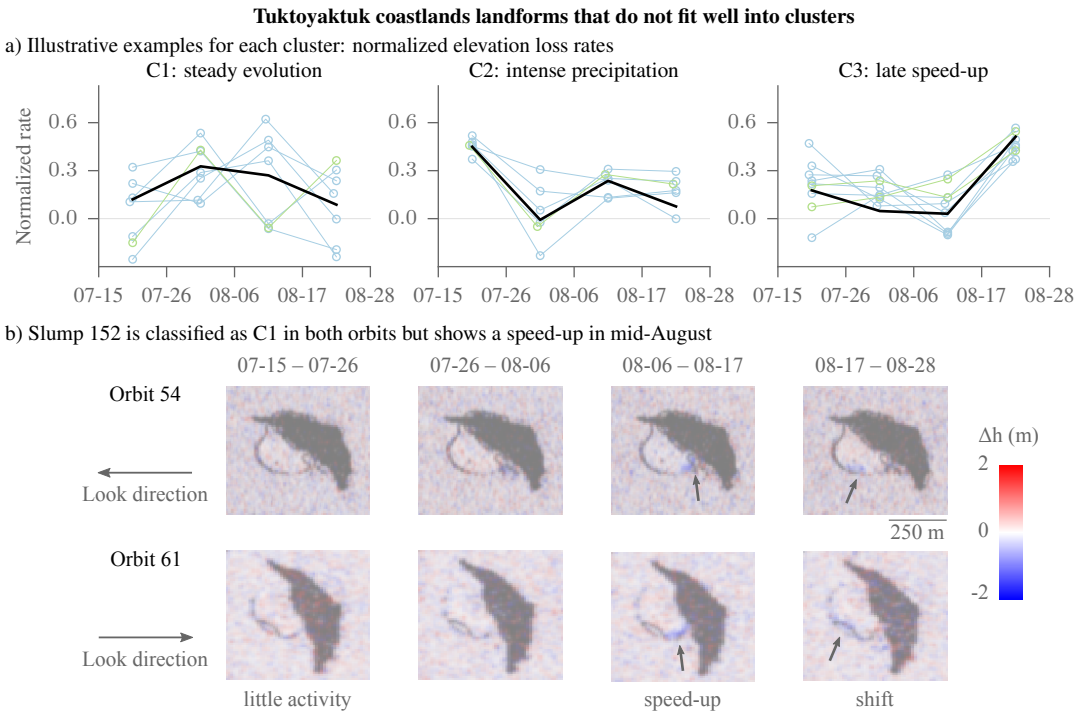

Figure S10: Examples of landforms in the Tuktoyaktuk coastlands that do not fit well into the clusters. a) Examples arranged according to the three clusters that they are assigned to (cf. Fig. 4). b) Slump 152, which was imaged from both sides, shows a speed-up in mid-August (like C2) but not in mid July (unlike C2) and is classified as C1. The spatial (arrows) and local patterns of activity match well in the images from both orbits (shown in radar coordinates, range direction horizontal).

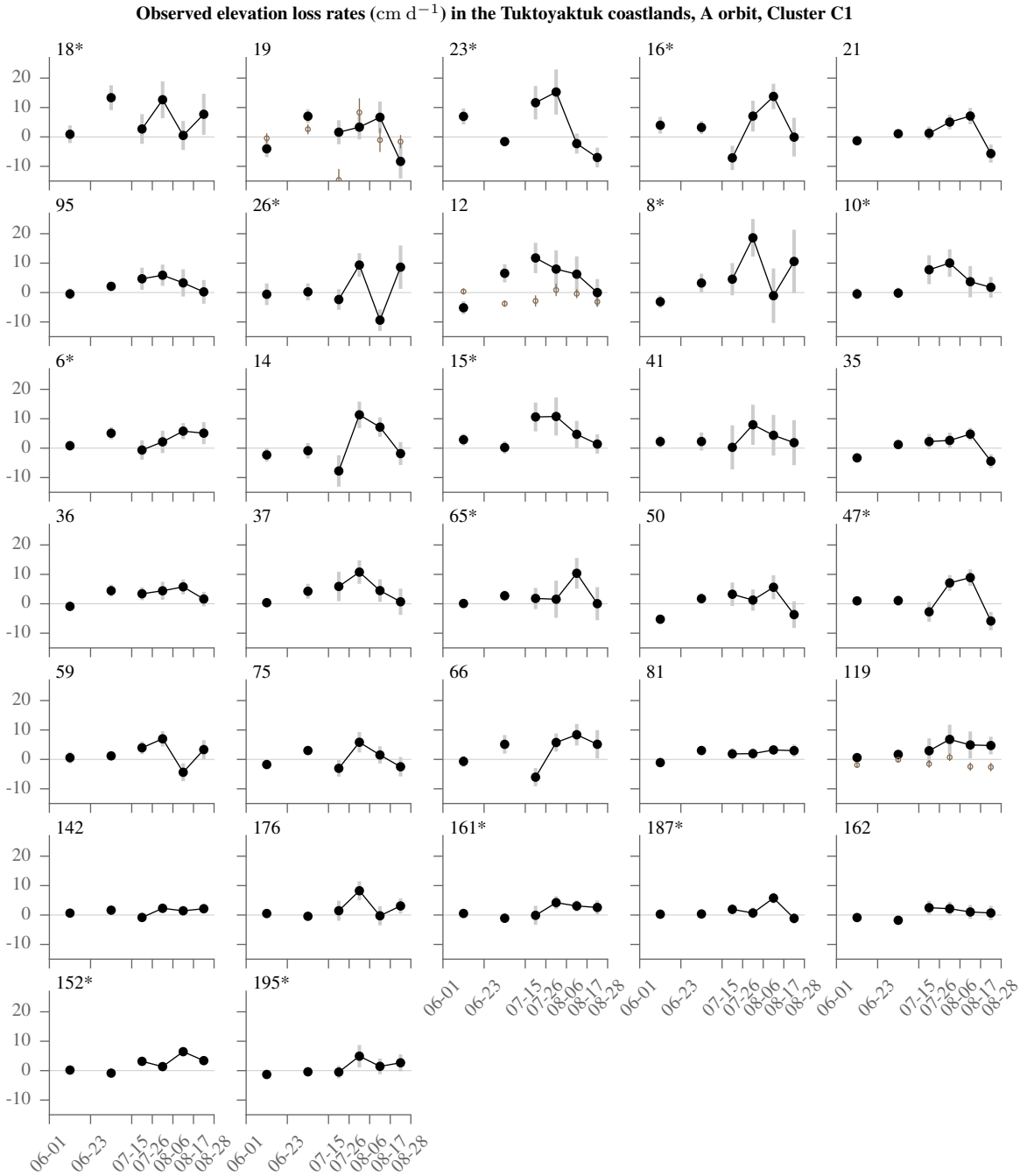

Figure S11: Observed elevation loss rates at slumps with detectable activity covered by the ascending orbit whose elevation loss dynamics in the second half of summer were classified as C1. For each slump, the number in the upper left gives the number, a star indicates a significant deviation from uniform dynamics after mid-July, and the plot shows the elevation loss at slump headwalls (aggregated median rate: black circle, standard error: grey error bars; horizontal position: between two subsequent radar acquisitions) and, where detected, at slump floors (median: brown circle, standard error: brown error bar; negative values indicate elevation increases). The dates in 2015 are plotted on the horizontal axis, with each tick representing a radar acquisition.

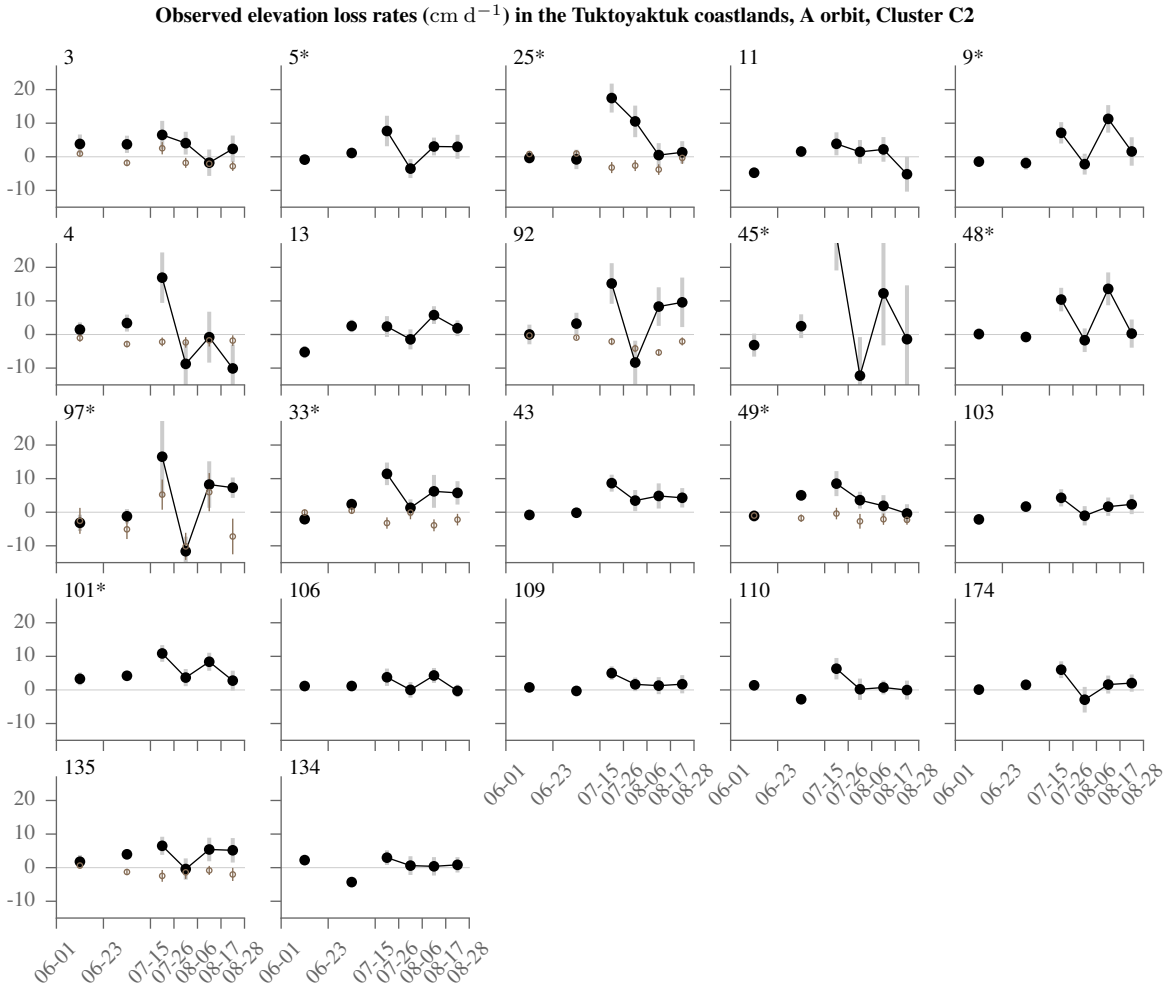

Figure S12: Same as Fig. S11 but for cluster C2.

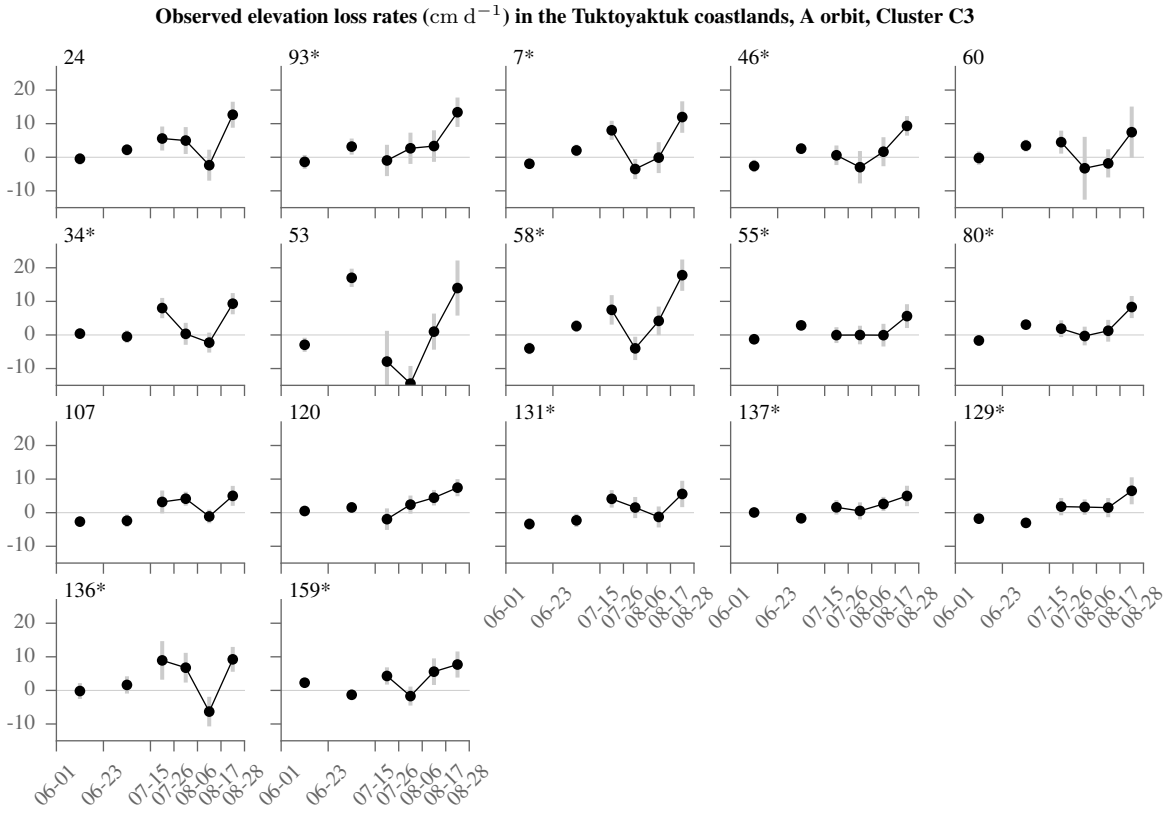

Figure S13: Same as Fig. S11 but for cluster C3.

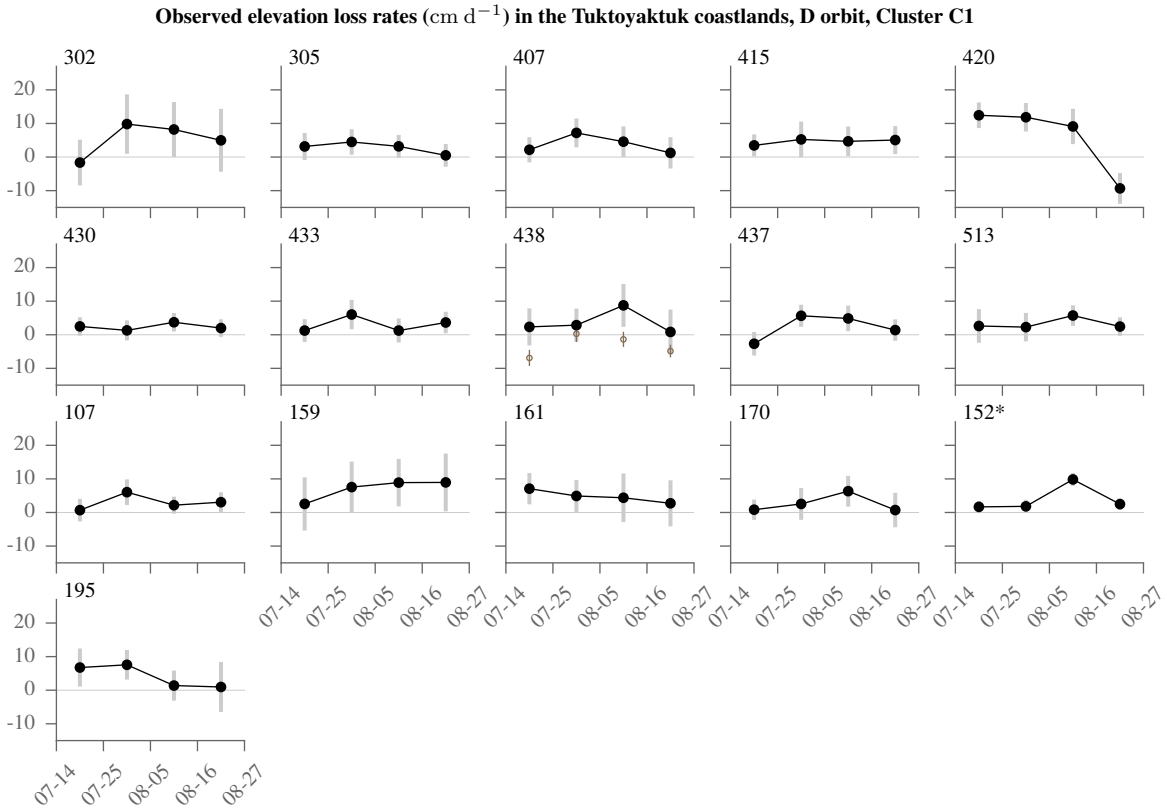

Figure S14: Same as Fig. S11 but for the descending orbit.

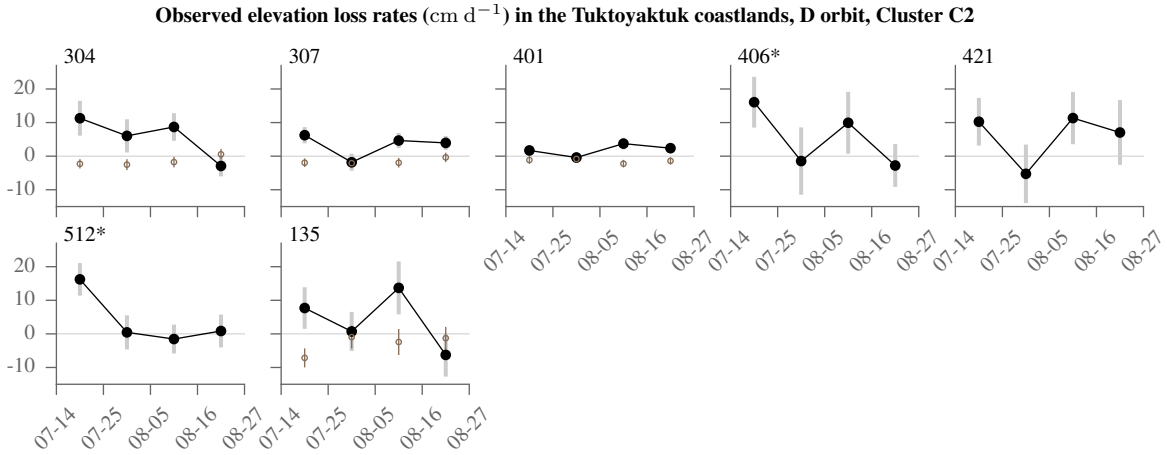

Figure S15: Same as Fig. S14 but for cluster C2.

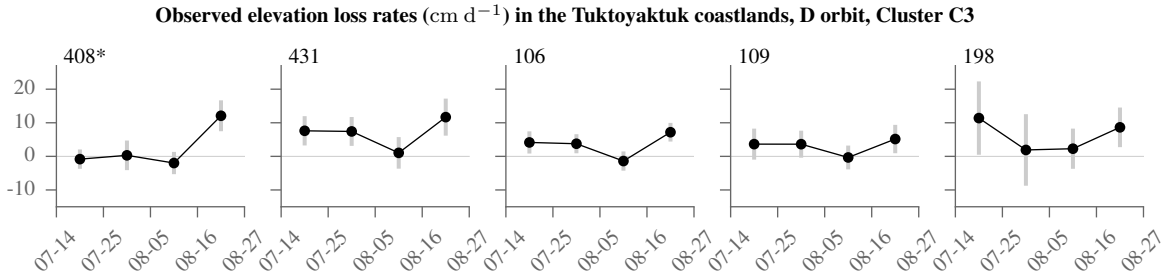

Figure S16: Same as Fig. S14 but for cluster C3.

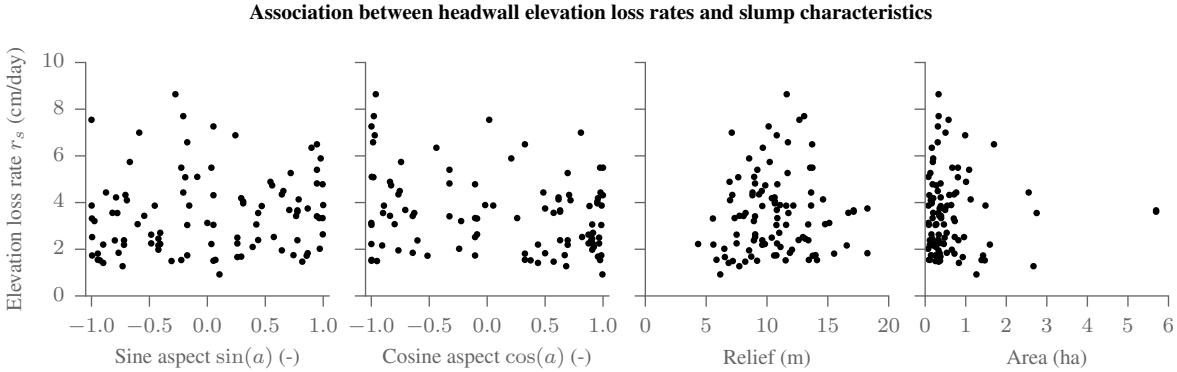

Figure S17: Headwall elevation loss rates in the Tuktoyaktuk Coastlands and how they are associated with slump characteristics. The data and the characteristics are identical to those in Fig. 5.

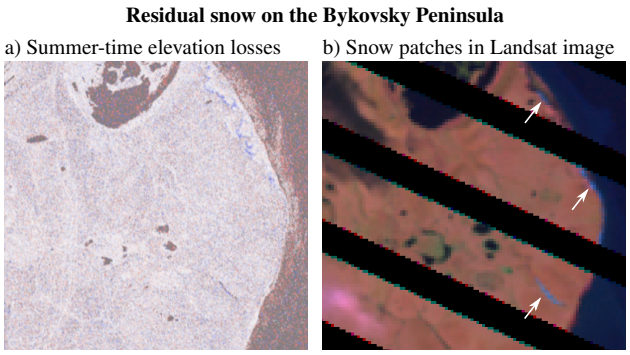

Figure S18: Residual snow cover potentially induced biases in the TanDEM-X elevation change estimates in early summer on the Bykovsky peninsula. a) Elevation loss rate r_s: this is a detail (identical colour code) of Fig. 6 around inset c2. b) False-colour Landsat-7 image (30 m resolution) from 09 July that shows snow patches in light blue (white arrows). The black stripes are gaps without data caused by sensor malfunction. A more exhaustive mapping was not possible owing to cloud cover, even on 09 July: the pink patch on the lower left is a cloud.

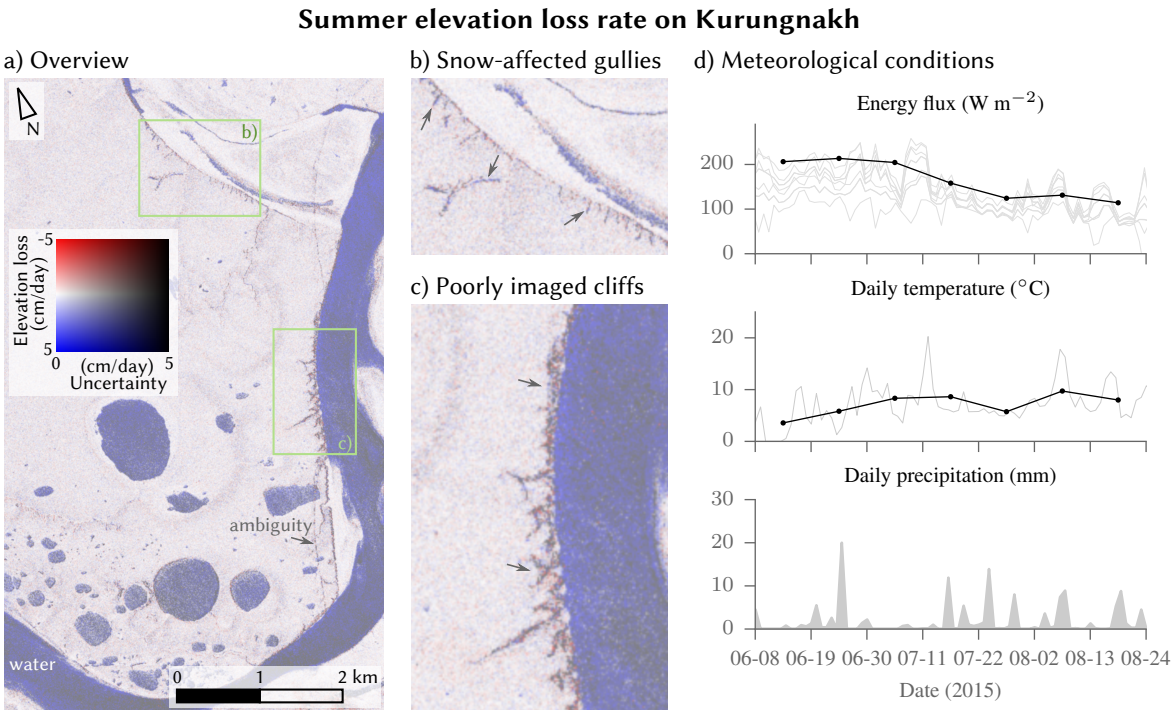

Figure S19: a) Observed elevation losses on Kurungnakh Island in radar coordinates (slant range from right to left), using the same colour code as in Fig. 3. The stacked rate r_s was estimated from acquisitions between 11 July and 24 August, after the ablation of most late-lying snow banks. However, snow is suspected to have caused the apparent subsidence in gullies (inset b). The layover-affected viewing geometry induced a poor imaging quality of the cliffs in the east (inset c) as well as an azimuth ambiguity. Note the spurious signal over water bodies. d) Meteorological forcing measured at Stolb station (12 km from Kurungnakh).

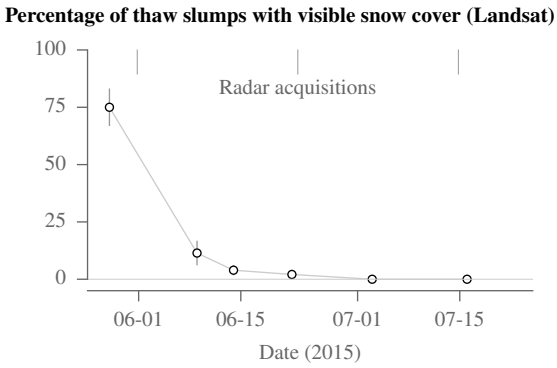

Figure S20: Disappearance of snow cover at slumps in the Tuktoyaktuk coastlands. The markers show the proportion of slumps at which snow cover could be detected in Landsat 7/8 panchromatic images (15m resolution) along with the estimated standard error (error bar). The error estimate did not account for the biased sampling as only certain regions where imaged and not obscured by clouds for each day. The vertical lines at the top show the dates of the TanDEM-X acquisitions.

References

[1] A. C. Davison and D. V. Hinkley. *Bootstrap Methods and their Application*. Cambridge University Press, 1997.

[2] A. Dehecq, R. Millan, E. Berthier, N. Gourmelen, E. Trouv, and V. Vionnet. Elevation changes inferred from TanDEM-X data over the Mont-Blanc area: Impact of the X-band interferometric bias. *IEEE Journal of Selected Topics in Applied Earth Observations and Remote Sensing*, 9(8):3870–3882, Aug 2016.

[3] S. J. Frasier and A. J. Camps. Dual-beam interferometry for ocean surface current vector mapping. *IEEE Transactions on Geoscience and Remote Sensing*, 39(2):401–414, Feb 2001.

[4] X. Golay, S. Kollias, T. Stoll, D. Meier, A. Valavanis, and P. Boesiger. A new correlation-based fuzzy logic clustering algorithm for fMRI. *Magnetic Resonance in Medicine*, 40(2):249–260, 1998.

[5] C. Gonzalez and B. Brutigam. Relative height accuracy estimation method for InSAR-Based DEMs. *IEEE Journal of Selected Topics in Applied Earth Observations and Remote Sensing*, 8(11):5352–5360, Nov 2015.

[6] G. Krieger, A. Moreira, H. Fiedler, I. Hajnsek, M. Werner, M. Younis, and M. Zink. TanDEM-X: A satellite formation for high-resolution SAR interferometry. *IEEE Transactions on Geoscience and Remote Sensing*, 45(11):3317–3340, 2007.

[7] T. C. Lantz, P. Marsh, and S. V. Kokelj. Recent shrub proliferation in the Mackenzie Delta uplands and microclimatic implications. *Ecosystems*, 16(1):47–59, 2013.

[8] W. T. Liao. Clustering of time series data—a survey. *Pattern Recognition*, 38:1857–1874, 2005.

[9] M. P. Poland. Time-averaged discharge rate of subaerial lava at Kilauea volcano, Hawaii, measured from TanDEM-X interferometry: Implications for magma supply and storage during 2011-2013. *Journal of Geophysical Research: Solid Earth*, 119(7):5464–5481, 2014. 2014JB011132.

[10] P. Rizzoli, B. Bräutigam, T. Kraus, M. Martone, and G. Krieger. Relative height error analysis of TanDEM-X elevation data. *ISPRS Journal of Photogrammetry and Remote Sensing*, 73:30 – 38, 2012.

[11] S. Solberg, D. J. Weydahl, and R. Astrup. Temporal stability of X-band single-pass InSAR heights in a spruce forest: Effects of acquisition properties and season. *IEEE Transactions on Geoscience and Remote Sensing*, 53(3):1607–1614, March 2015.

[12] S. Suchandt and H. Runge. Ocean surface observations using the TanDEM-X satellite formation. *IEEE Journal of Selected Topics in Applied Earth Observations and Remote Sensing*, 8(11):5096–5105, Nov 2015.

[13] A. J. Wilkinson. Synthetic aperture radar interferometry: a model for the joint statistics in layover areas. In *Proceedings of the 1998 South African Symposium on Communications and Signal Processing, 1998.*, pages 333–338, Sep 1998.